Acoustic Ghost Imaging in the Time Domain

Yuan Tian,[1] Hao Ge,[1] Xiu-Juan Zhang,[1] Xiang-Yuan Xu,[1,2] Ming-Hui Lu,[1,3,*] Yun Jing,[4,5,†] and Yan-Feng Chen[1,3]

[1] *National Laboratory of Solid State Microstructures and Department of Materials Science and Engineering, Nanjing University, Nanjing, 210093 Jiangsu, China*

[2] *The Institute of Acoustics of the Chinese Academy of Sciences, 100190 Beijing, China*

[3] *Collaborative Innovation Center of Advanced Microstructures, Nanjing, 210093 Jiangsu, China*

[4] *Department of Mechanical and Aerospace Engineering, North Caroline State University, Raleigh, North Carolina 27695, USA*

[5] *Graduate Program in Acoustics, The Pennsylvania State University, University Park, Pennsylvania 16802, USA*

(Received 30 October 2019; revised manuscript received 3 March 2020; accepted 15 May 2020; published 18 June 2020)

Ghost imaging (GI) enables reconstruction of the image of an object by measuring the intensity correlation of two beams, neither of which independently carries the spatial characteristics of the object. By exploiting the space-time duality, GI has been extended from the spatial domain to the time domain, and has been successfully demonstrated in the optical regime. This article reports on the experimental demonstration of acoustic GI in the time domain. Using ultrasound instead of photons, we created high-quality ghost images of a temporal object, even in the presence of strong ambient noise. Our work offers a fresh approach for imaging disturbance-sensitive acoustic signals, and could open the gateway to identifying new approaches in acoustic sensing, dynamic imaging, and communications.

DOI: 10.1103/PhysRevApplied.13.064044

I. INTRODUCTION

Ghost imaging (GI) is an emerging technique that is capable of reconstructing the image of an object by correlating the intensity of two beams of light (i.e., a reference beam and a test beam). The reference beam does not interact with the object and is directly recorded by a high-resolution detector (e.g., a camera). The test beam, after passing through the object, is detected by a non-spatially-resolved bucket detector. Aggregating the correlations between the two detectors over multiple measurements produces an image of the object, although neither detector alone is able to reveal the spatial characteristics of the object [1].

Initially demonstrated in 1995 with entangled photon pairs [2], GI was thought to be a quantum phenomenon. Later, thermal [3,4] and pseudothermal [5] GI were achieved and suggested that GI could also be realized in classical systems. Subsequently, GI has been applied to an expanded range of illumination types, including classical or quantum light [2–5], x rays [6–8], atoms [9], and electrons [10]. In particular, computational GI [11] uses a computer-controlled spatial light modulator to generate known illumination fields, which removes the need for imaging the reference beam. Based on the space-time duality, the concept of GI has been further extended from the spatial domain to the time domain. Temporal ghost imaging (TGI) was experimentally confirmed with use of an optical-fiber-based system [12]. A variety of light sources, including biphoton states [13], lasers [14,15], and computer-generated random light [16], have been harnessed to realize TGI. These developments in GI have benefited several applications, such as environmental sensing [17], cryptography [18], ultrafast spectroscopy [19], and low-light-level imaging [20]. However, TGI has been demonstrated only in the optical regime [12–16], and there is no acoustic counterpart of this promising imaging method.

As an important carrier of energy and information, acoustic waves play an important role in areas including communication [21,22], medical imaging [23], and localization and detection [24,25]. Although acoustic signals can be directly detected by sensors, it is challenging to decode useful information carried by the wave in the case of low signal-to-noise ratios (SNRs). To solve this grand challenge, it is highly desirable to develop an acoustic measurement technique that is robust with regard to noise. The recent developments in GI may offer an elegant solution to detect and recover acoustic signals with low SNRs.

*luminghui@nju.edu.cn

†jing.yun@psu.edu

 © 2020 American Physical Society

This article reports on an experimental demonstration of acoustic GI in the time domain. We show that the correlation between the computer-generated random intensity fluctuations and the bucket measurement enables the reconstruction of a temporal object, and this method is able to recover the object information even in the presence of strong ambient noise. Based on frequency multiplexing, acoustic single-shot TGI has also been realized, and is capable of imaging nonreproducible temporal objects. Our work, therefore, constitutes a major step toward introducing GI techniques into the acoustic regime, which could broaden the application of this imaging modality to facilitate acoustic communications, dynamic imaging, and remote sensing.

II. EXPERIMENTAL RESULTS

A. Illustration of acoustic temporal ghost imaging

The principle of TGI is illustrated in Fig. 1(a). The signals emitted from the source with random intensity fluctuations split into two arms. In one arm, the signals interact with the object and are subsequently detected by a bucket detector, whose response is integrated over a period of time. In the other arm, the signals that do not interact with the temporal object are collected with a proper temporal resolution. Finally, the temporal object is reconstructed by calculating the correlations between the temporal intensity fluctuation and the response of the bucket detector. In optics, for example, the intensity fluctuation can be produced by leveraging the intrinsic temporal fluctuation of laser light. In this work, acoustic illumination signals are directly controlled by a computer that generates known random patterns. This removes the need for detecting the reference beam, which is the core of computational GI. Additionally, because of the innate difference between acoustic and optical measurements, there is no analog of a temporal bucket detector in acoustics. We therefore integrate the acoustic intensity over time to emulate the response of a bucket detector, and this operation is defined here as the bucket measurement.

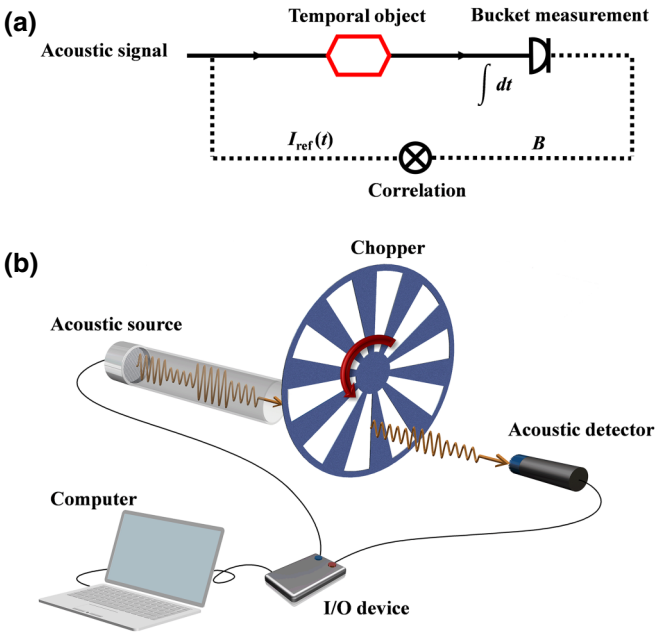

FIG. 1. Illustration of acoustic temporal ghost imaging. (a) The principle of temporal ghost imaging. (b) Experimental setup. The ultrasonic waves emitted by the acoustic source illuminate the temporal object (a chopper in this case) with computer-generated random intensity fluctuations. The acoustic signals through the object are collected by an acoustic detector and subsequently the bucket measurement is performed. The known random intensity and the information from the bucket measurement are finally used to reconstruct the temporal object.

The experimental setup for the acoustic TGI is illustrated in Fig. 1(b). An ultrasonic transducer is used as the acoustic source, and the waves emitted at a frequency of 25 kHz are confined in a rigid tube. The random intensity fluctuation of the acoustic waves is controlled by the computer. At the end of the tube, a rotating chopper, whose chopping frequency is 20 Hz, is placed and periodically interacts with the incident acoustic waves. This chopper is the temporal object, and its sound transmission $T(t)$ is to be imaged. The transmitted acoustic signals are measured by a detector (Brüel & Kjær 4939 0.25-in. microphone), followed by the bucket measurement, whose reading is calculated as B, which is the integrated intensity of the transmitted signals over a period of time (200 ms). The experimental setup also includes a computer to generate and record the random intensity patterns as well as to reconstruct the ghost image. A multifunction I/O device (National Instruments PCI-6251) controlled by the computer is used for signal generation and acquisition. It sends sinusoidal signals with intensity fluctuations to the acoustic source, and collects signals from the acoustic detector to feed to the computer.

The acoustic signals emitted from the ultrasonic transducer produce computer-generated random intensity patterns as shown in Fig. 2(a). The red line shows one of the patterns, while the gray background is the result of 50 patterns being superimposed on top of each other. The black line is the intensity averaged over 9000 measurements. As can be seen, the intensity of the signal is temporally randomized in a way that it possesses the statistical property of a uniform distribution. The signal corresponding to the random intensity pattern of the red line is shown in Fig. 2(b), whose effective fluctuation time is 4 ms. Here the effective fluctuation time is the duration of sinusoidal signals with constant intensity. It directly determines the temporal resolution of ghost image and must be shorter than the object variation that we desire to resolve.

According to the GI theory, the object information can be retrieved with the second-order intensity correlation

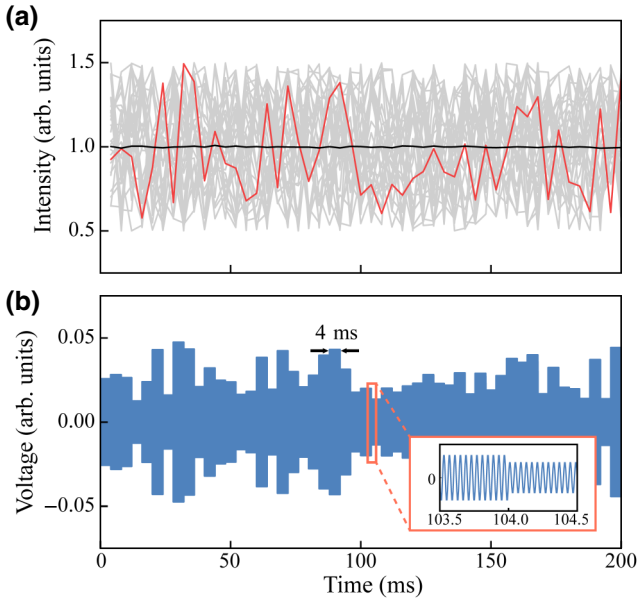

FIG. 2. (a) Computer-generated random intensity patterns of the acoustic illumination signals. A single realization (red) is shown together with 50 other realizations (gray). The averaged intensity of 9000 measurements is shown as the black line. (b) The signal corresponding to the random intensity pattern of the red line, which is sent to the acoustic source.

function defined as [25]

$$C(t) = \langle I^i_{\mathrm{ref}}(t) B^i \rangle_N - \langle I^i_{\mathrm{ref}}(t) \rangle_N \langle B^i \rangle_N, \tag{1}$$

where $I^i_{\mathrm{ref}}(t)$ is the time-resolved intensity of the illumination signal at time t in the ith measurement, which is the reference signal and is known as a "prior"; B^i is the integrated intensity from the bucket measurement, denoted the bucket signal; $\langle \ldots \rangle_N$ represents the ensemble average over a series of N measurements, and $I^i_{\mathrm{ref}}(t)$ can also be formulated by a $1 \times M$ vector $\mathbf{X}_i$ (see more-detailed matrix operation of TGI in Appendix B).

B. Experimental ghost images

Using Eq. (1), we obtain the temporal ghost image (Fig. 3) from a series of measurements ($N = 9000$). Our target image, the result of a direct image without noise (details are given in Appendix A), is shown as the black line in Fig. 3 for comparison. Normalization is applied for both images, and the agreement between the two is excellent. In our experiments, the temporal resolution of the ghost image is 4 ms, which is identical to the effective fluctuation time of the illumination signal. In our case, the period of the temporal object is 50 ms, which is much longer than 4 ms. Consequently, the resulting ghost image can capture the temporal characteristics of the object.

Figure 4(a) compares the ghost images for different numbers of measurements. It is difficult to recognize the

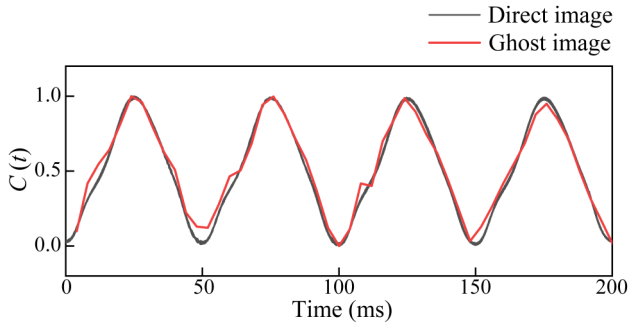

FIG. 3. Experimental ghost image of a temporal object. The red line represents the ghost image and the black line shows the direct image. The number of measurements N for the ghost image is 9000.

temporal characteristics of the object when N is a small quantity such as 50. To quantitatively evaluate the ghost-image quality, we introduce the peak signal-to-noise ratio (P_{SNR}) as

$$P_{\mathrm{SNR}} = 10 \log_{10} \left(\frac{M^2_{\mathrm{max}}}{M_{\mathrm{mse}}} \right), \tag{2}$$

where M_{max} is the maximum pixel value of the image; normalization is applied in calculating the P_{SNR}, giving M_{max}

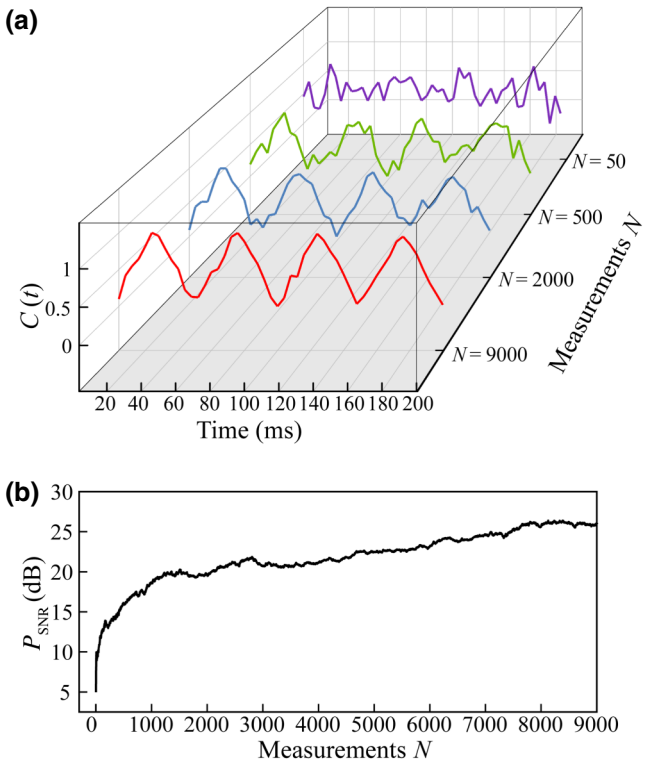

FIG. 4. Ghost image and the P_{SNR} as a function of the number of measurements N. (a) Experimental ghost images for different N. (b) P_{SNR} with N ranging from 1 to 9000.

of 1. $M_{\rm mse}$ is the mean square error given by

$$M_{\rm mse} = \frac{1}{L}\sum_i [C(i) - T(i)]^2, \tag{3}$$

where $C(i)$ and $T(i)$ are the pixel values of the ghost image and the target image, and L is the number of pixels in the signal. The $P_{\rm SNR}$ values for measurements corresponding to $N = 50$, 500, 2000, and 9000 are calculated as 10.48, 15.97, 19.65, and 26.02 dB, respectively. Furthermore, $P_{\rm SNRs}$ of ghost images for different values of N from 1 to 9000 are shown in Fig. 4(b). One can clearly see that the quality of the ghost images improves as N increases.

C. Comparison of correlation algorithms

In the GI technique, the correlation algorithm mainly determines the efficiency of the image-reconstruction process and the quality of the image. Although we use the second-order correlation function to verify the acoustic TGI, there are many other existing algorithms that can further improve the imaging result [26–30]. Here we introduce two other algorithms for our case—differential ghost imaging (DGI) and pseudoinverse ghost imaging (PGI)—to compare the imaging results among different algorithms.

In the DGI algorithm, a differential bucket signal is used for correlation calculation, which is defined as

$$B^i_{\rm DGI} = B^i - \frac{\langle B^i\rangle}{\langle S^i\rangle}S^i, \tag{4}$$

where $S^i = \int I^i_{\rm ref}(t)dt$ is the total intensity of the reference signal or the sum of the random row vector $\mathbf{X}_i$. The reconstruction algorithm can be expressed as

$$C_{\rm DGI}(t) = \langle I^i_{\rm ref}(t)B^i_{\rm DGI}\rangle_N - \langle I^i_{\rm ref}(t)\rangle_N\langle B^i_{\rm DGI}\rangle_N. \tag{5}$$

On the other hand, in the PGI algorithm, the reference information is permutated into an $N \times M$ matrix $\mathbf{\Phi}$; that is, $\mathbf{\Phi} = [\mathbf{X}_1, \mathbf{X}_2, \ldots, \mathbf{X}_N]^T$. We reconstruct the object information by calculating the pseudoinverse of $\mathbf{\Phi}$ and the algorithm is formulated as

$$\mathbf{C}_{\rm PGI} = \frac{1}{N}\mathbf{\Phi}^\dagger(B^1, B^2, \ldots, B^N)^T, \tag{6}$$

where $\mathbf{\Phi}^\dagger$ is the pseudoinverse matrix of $\mathbf{\Phi}$.

Figure 5 shows the ghost images reconstructed by our using the three different algorithms for $N = 200$ in the experiment. The $P_{\rm SNR}$ values for GI, DGI, and PGI are calculated as 12.79, 16.63, and 22.13 dB, respectively. The comparison in Fig. 5 suggests that DGI and PGI offer better quality and higher reconstruction efficiency than traditional GI.

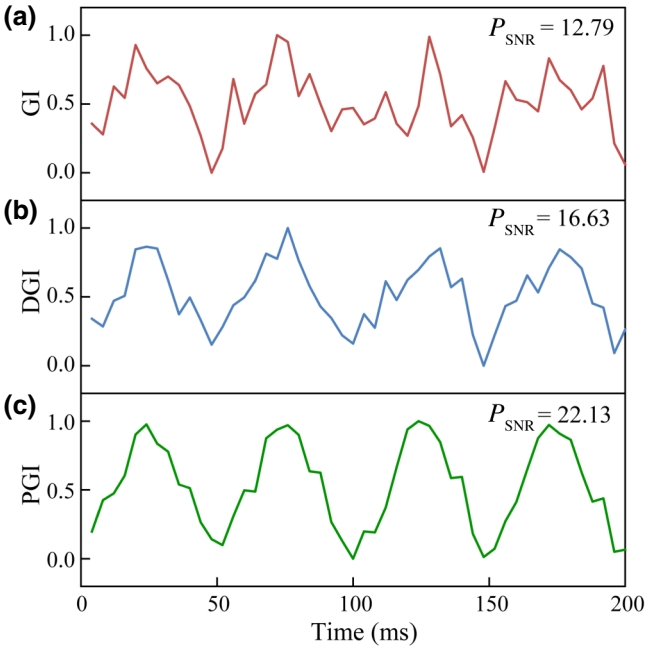

FIG. 5. Experimental results with different reconstruction algorithms: (a) traditional GI; (b) DGI; (c) PGI. The number of measurements N is 200 for all three cases.

D. Robustness of acoustic temporal ghost imaging

GI is insensitive to the disturbance near the objects to be imaged and has been shown to be more robust than noncorrelated imaging. This remarkable feature is especially useful for imaging objects under strong background disturbances such as atmospheric turbulence and scattering media [31–33]. We now investigate the robustness of acoustic TGI with regard to the ambient noise. In the experiment, white noise signals are created by a signal generator (Tektronix AFG 3252C) and are sent to a loudspeaker via a power amplifier (Brüel & Kjær type 2713). Both the ghost image and the direct image are subsequently obtained for comparison.

Figure 6 clearly shows that a direct measurement of the temporal object is strongly distorted by the background noise. However, when the GI technique is used, the adverse effect of the noise is significantly suppressed and has virtually no influence on the quality of the ghost image (GI results for two other temporal objects are presented in Appendix C). Furthermore, under different noise levels (with a 10-dB increasing increment), images of the temporal object are obtained with both methods, as shown in Fig. 7(a). The $P_{\rm SNR}$ values of these images are shown in Fig. 7(b). The quality of the direct images decreases dramatically with increasing noise level, while increasing noise level has negligible influence on the quality of the

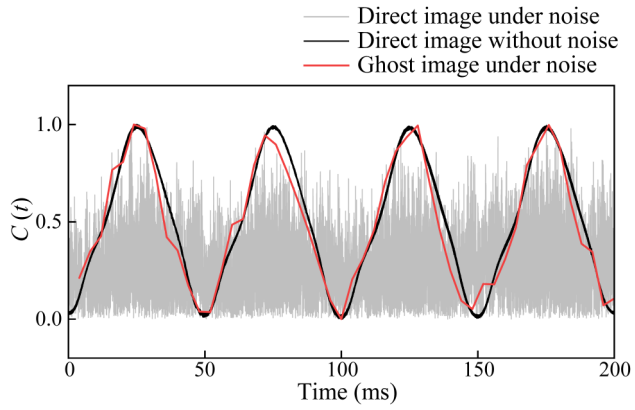

FIG. 6. Experimental comparison of ghost image (red) and direct image (gray) in the presence of ambient noise. For comparison, the direct image obtained without noise is also shown in black. The number of measurements N for the ghost image is 9000.

ghost images. Thus, acoustic GI in the time domain shows considerably greater robustness with regard to noise than direct measurement (the detailed analysis of the robustness of TGI is presented in Appendix D).

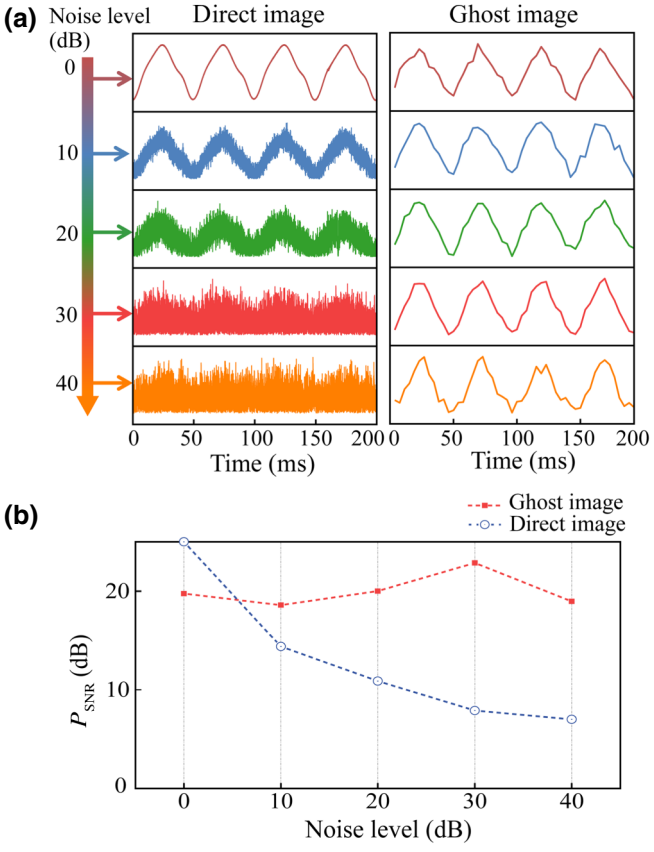

FIG. 7. Experimental imaging results for different noise levels. (a) The direct images (left) and the ghost images (right). From top to bottom, the strength of ambient noise increases. (b) P_{SNR} of both images for different noise levels.

E. Single-shot temporal ghost imaging

Generally, GI requires multiple measurements of the object; therefore, TGI typically requires the object to be periodic in nature. To image nonperiodic signals, space multiplexing [16,34,35] and frequency (wavelength) multiplexing [36] can be used to realize single-shot TGI, which allows us to retrieve a temporal object by using a single correlation measurement. Here we experimentally demonstrate that our acoustic system can achieve single-shot TGI using frequency multiplexing.

With the same experimental setup as shown in Fig. 1, the acoustic wave emitted from the source is no longer a single-frequency signal but is rather a broadband one. We use a 20×20 Hadamard matrix as the frequency-localized temporal intensity pattern to encode different frequency components of the emitted signal. The number of frequency components is equivalent to the number of measurements of standard TGI. Figure 8(a) shows the emitted signal (20.5–30 kHz) and Fig. 8(b) shows the Hadamard matrix, which is the reference signal and represents the time-frequency information of the emitted signal. After the acoustic wave passes through a temporal object, the fast Fourier transform is used to decode the transmitted signal to obtain the bucket signal (i.e., the integrated intensity of the transmitted signal at each frequency). Finally, we use the same correlation function as in Eq. (1) to obtain

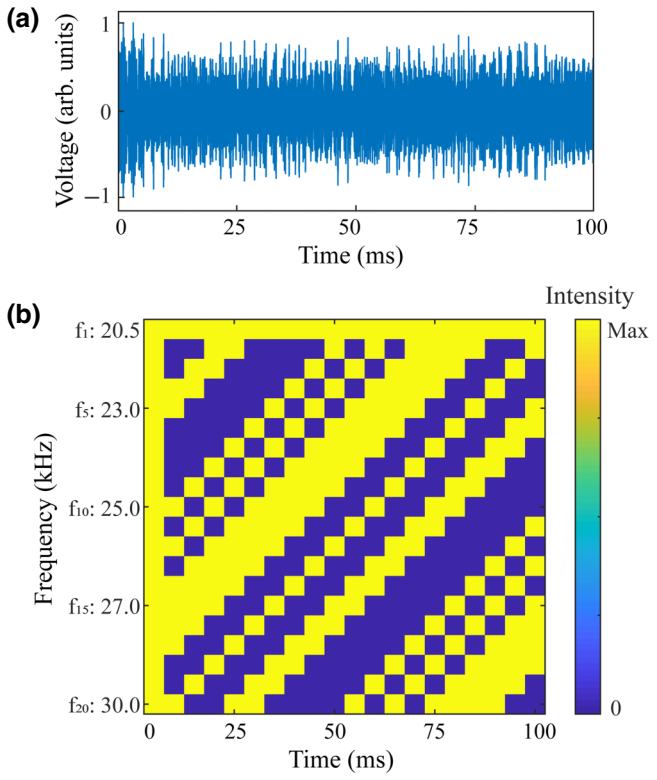

FIG. 8. (a) The encoded incident signal. (2) 20×20 Hadamard matrix. The matrix is used to encode the emitted signal.

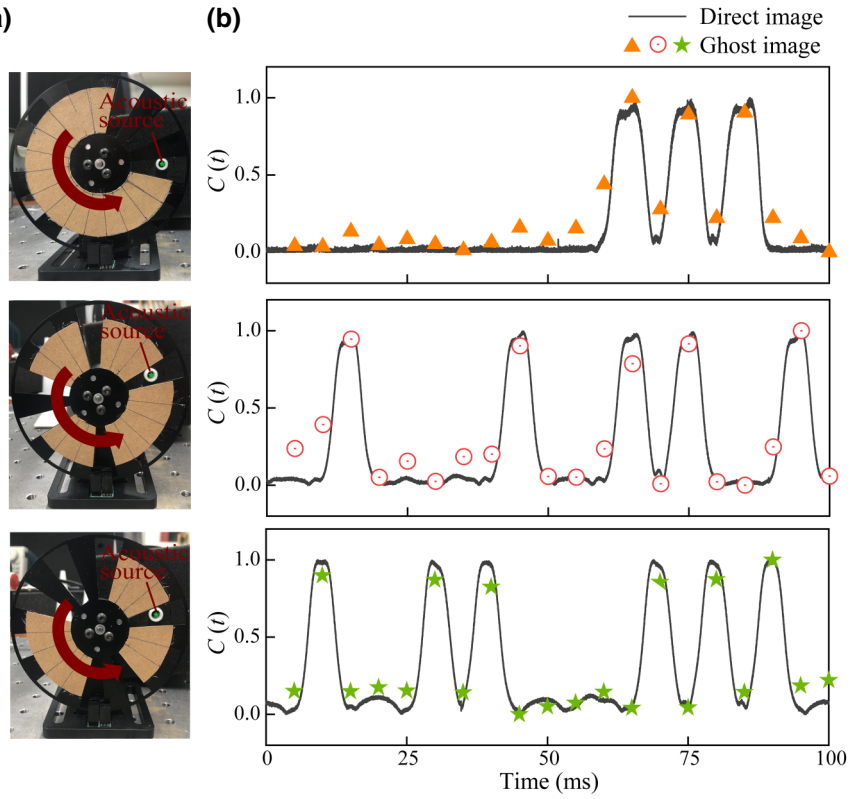

FIG. 9. Experimental ghost images of different nonperiodic signals. (a) Photographs of three different choppers. We code the shape of the chopper and then use it to create nonperiodic signals. (b) Experimental results of single-shot ghost imaging.

the ghost image of the temporal object. In this case, $I^i_{\mathrm{ref}}(t)$ is the time-resolved intensity of the illumination signal at the ith frequency.

In this experiment, we create three different nonperiodic signals by coding the shape of the chopper, as shown in Fig. 9(a). The retrieved ghost images are shown in Fig. 9(b), and their temporal resolution is 5 ms. Good agreement between ghost images and direct images is found. These results demonstrate that our system can reconstruct high-quality images, with a single measurement, for nonperiodic signals.

III. CONCLUSION

In conclusion, our experiments successfully demonstrate acoustic GI in the time domain. In addition to showing high-quality ghost images of a temporal object, our results also suggest that acoustic TGI is extremely robust with regard to background noise. This technique, therefore, can prove useful for detecting and recovering acoustic signals with low SNRs for better sound recognition. Based on frequency multiplexing, acoustic single-shot TGI is realized, which could facilitate real-time signal detection. Acoustic TGI also offers an economic and versatile platform for studying correlated imaging algorithms, offering great promise for applications in acoustic sensing, signal processing, information encryption [37,38], and underwater communications. Finally, our work paves the way for further development of other acoustic GI modalities, such as acoustic spatial GI and acoustic ghost spectroscopy.

ACKNOWLEDGMENTS

This work was jointly supported by the National Key R&D Program of China (Grants No. 2016YFB0700301, No. 2017YFA0303702, and No. 2018YFA0306200) and the National Natural Science Foundation of China (Grants No. 51732006, No. 11625418, No. 11474158, and No. 11890700). We also acknowledge funding from the Priority Academic Program Development of Jiangsu Higher Education (PAPD).

APPENDIX A: DETAILS OF DIRECT IMAGING OF THE TEMPORAL OBJECT

The chopper as the temporal object is shown in Fig. 10(a) and its sound transmission $T(t)$ is regarded as our imaging target. The transmitted acoustic signals are measured by a detector, recorded as $V_r(t)$. The wave packet of $V_r(t)$, which is consistent with the characteristics of the intensity transmission $T(t)$, can be extracted as $D(t) = [V_r(t)^2 + V_i(t)^2]^{1/2}$, in which $V_i(t) = H[V_r(t)] = \int [1/\pi(t - t')]V_r(t')dt'$, where H denotes the Hilbert transform. The image of $D(t)$ is the result of direct measurements (namely, the direct image), and it is shown in Fig. 10(b). However, the direct image can be often drowned out by the noise. This is demonstrated by comparing Figs. 11 and 12.

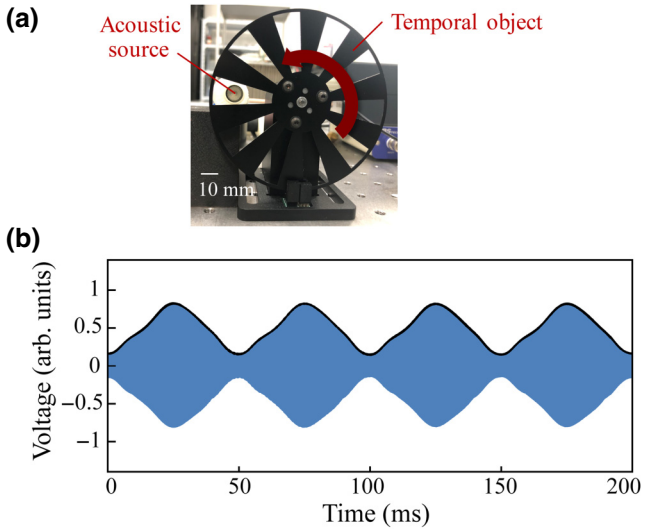

FIG. 10. (a) Photograph of the temporal object (i.e., a rotating chopper). (b) The direct image of the temporal object, which is the wave packet of the recorded transmission signal and is shown as the black line. The blue shading is the transmission signal.

APPENDIX B: THE MATRIX OPERATION OF ACOUSTIC TEMPORAL GHOST IMAGING

According to Eq. (1), we can also describe the second-order correlation function as matrix operations. If we let the total number of measurements be N and the number of imaging pixels be M, the temporal object can be expressed as a $1 \times M$ vector $\mathbf{O} = [O_1, O_2, \ldots, O_M]$. Similarly, the result of bucket measurements in the ith measurement is a scalar, defined as B_i. Likewise, the time-resolved reference intensity $I^i_{\mathrm{ref}}(t)$ in the ith measurement can be denoted by a $1 \times M$ vector $\mathbf{X}_i$ $(i = 1, 2, \ldots, N)$. The total reference information can be then permutated into an $N \times M$ matrix $\mathbf{\Phi} = [\mathbf{X}_1, \mathbf{X}_2, \ldots, \mathbf{X}_N]^T$, where T denotes the transpose of the matrix. Consequently, we have

$$B_i = \mathbf{O}\mathbf{X}_i^T.$$

Finally, the second-order correlation function can be computed by

$$\mathbf{C} = \langle \mathbf{X}_i B_i \rangle_N - \langle \mathbf{X}_i \rangle_N \langle B_i \rangle_N. \tag{B1}$$

In Eq. (B1), the first term $\langle \mathbf{X}_i B_i \rangle_N = \langle \mathbf{O}\mathbf{X}_i^T \mathbf{X}_i \rangle_N = (1/N)\,\mathbf{O} \cdot (\mathbf{\Phi}^T\mathbf{\Phi})$, and the second term $\langle \mathbf{X}_i \rangle_N \langle B_i \rangle_N = \langle \mathbf{X}_i \rangle_N \langle \mathbf{O}\mathbf{X}_i^T \rangle_N$, which is the background. Therefore, we have

$$\mathbf{C} = \frac{1}{N}\mathbf{O} \cdot (\mathbf{\Phi}^T\mathbf{\Phi}) - \langle \mathbf{X}_i \rangle_N \langle \mathbf{O}\mathbf{X}_i^T \rangle_N. \tag{B2}$$

Judging from Eq. (B2), only when $\mathbf{\Phi}^T\mathbf{\Phi}$ is a scalar matrix whose diagonal elements are identical will the ghost image of the temporal object be perfectly recovered.

It is seen in Fig. 13 that when the number of measurements increases, $\mathbf{\Phi}^T\mathbf{\Phi}$ is closer to a scalar matrix, which results in better quality of the ghost image (shown in Fig. 4).

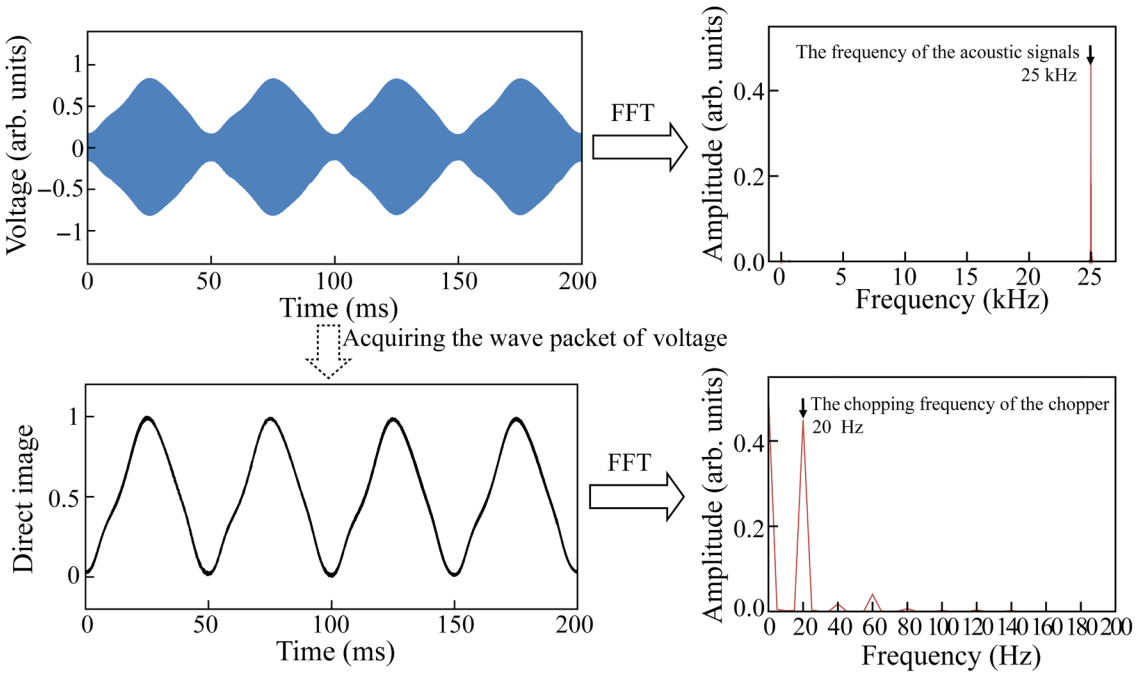

FIG. 11. The frequency spectrum of the directly recorded signals and the direct image without noise. FFT, fast Fourier transform.

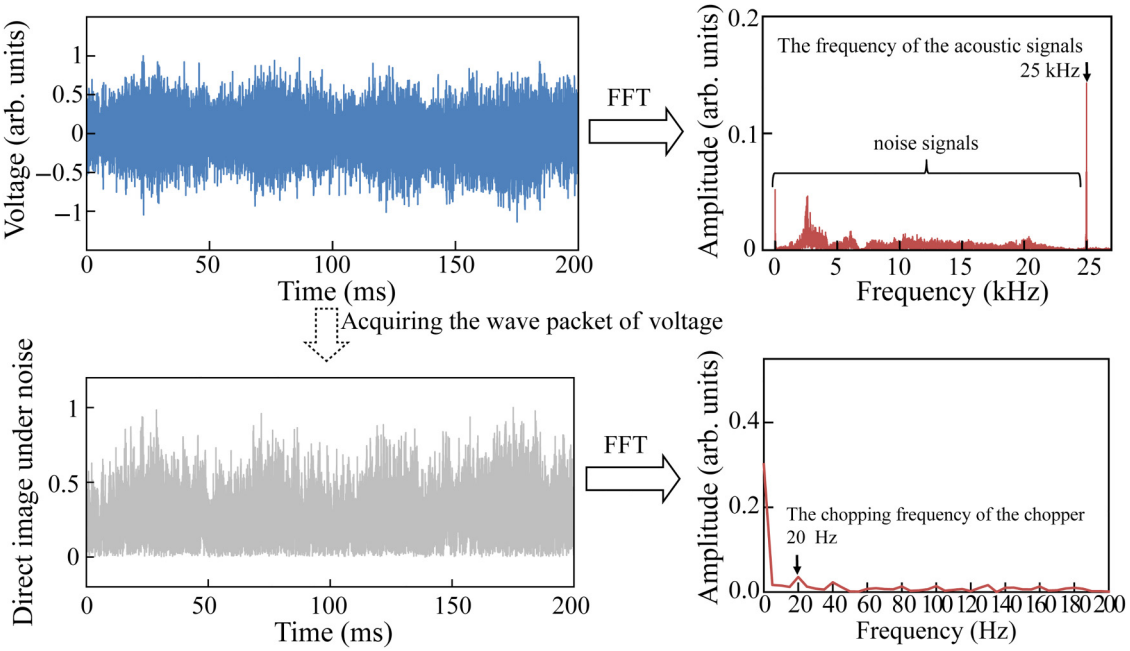

FIG. 12. The frequency spectrum of the directly recorded signals and the direct image under ambient noise. FFT, fast Fourier transform.

APPENDIX C: GHOST IMAGES OF OTHER TEMPORAL OBJECTS

Here we investigate GI results for other complex temporal objects, as shown in Fig. 14. In the experiment, ghost images are reconstructed under the noise condition. For comparison, direct images with or without noise are also shown in Fig. 14. We can also clearly recognize the temporal characteristics from the ghost images, whose quality is better than the quality of direct images obtained under the same noise condition.

APPENDIX D: THE ROBUSTNESS OF GHOST IMAGING WITH REGARD TO NOISE

Here we explain why GI is robust with regard to noise. First, we briefly review the process of GI without background noise. The reference signal is expressed as $I^i_{\mathrm{ref}}(t)$, while the temporal object to be reconstructed is expressed as $T(t)$. In the absence of background noise, the bucket signal is defined as B^i_0, where $B^i_0 = \int I^i_{\mathrm{ref}}(t')T(t')dt'$. The ghost image can be reconstructed by calculating the second-order correlation, defined as

$$C_0(t) = \langle I^i_{\mathrm{ref}}(t)B^i_0\rangle_N - \langle I^i_{\mathrm{ref}}(t)\rangle_N \langle B^i_0\rangle_N. \quad \text{(D1)}$$

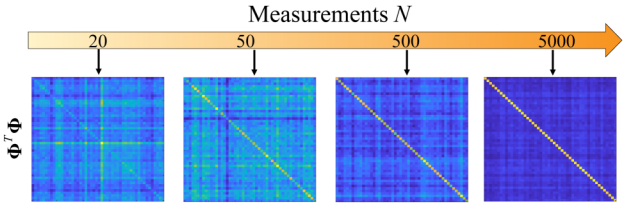

FIG. 13. Comparison of $\Phi^T\Phi$ for different numbers of measurements N.

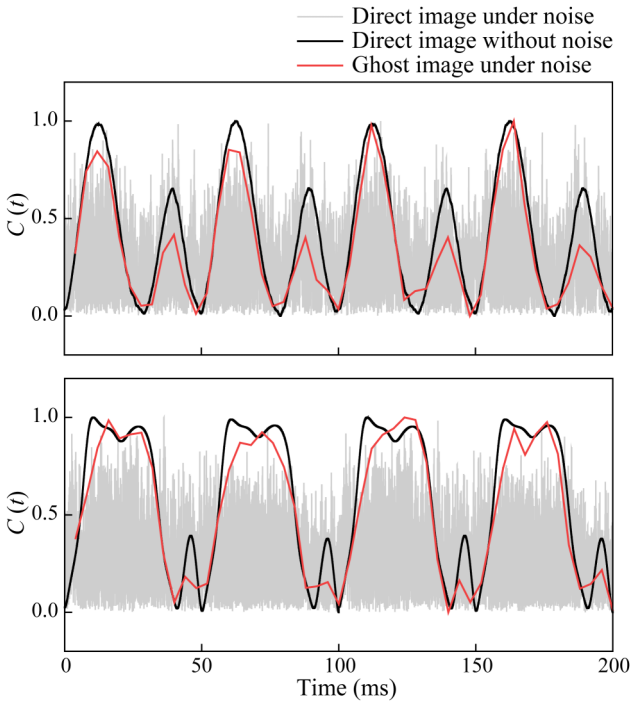

FIG. 14. Ghost images of two other temporal objects reconstructed by GI; the number of measurements N is 9000.

In the presence of background noise, the bucket signal is

$$B^i = \int I^i_{\mathrm{ref}}(t')T(t')dt' + \alpha \int I^i_{\mathrm{noise}}(t')dt' + \beta \int I^i_{\mathrm{noise}}(t')T(t')dt' = B^i_0 + B^i_{\mathrm{noise}}. \quad \text{(D2)}$$

Therefore, the ghost image under noise can be written as

$$\begin{aligned} C(t) &= \langle I^i_{\mathrm{ref}}(t)B^i\rangle_N - \langle I^i_{\mathrm{ref}}(t)\rangle_N\langle B^i\rangle_N \\ &= [\langle I^i_{\mathrm{ref}}(t)B^i_0\rangle_N - \langle I^i_{\mathrm{ref}}(t)\rangle_N\langle B^i_0\rangle_N] \\ &\quad + [\langle I^i_{\mathrm{ref}}(t)B^i_{\mathrm{noise}}\rangle_N - \langle I^i_{\mathrm{ref}}(t)\rangle_N\langle B^i_{\mathrm{noise}}\rangle_N] \\ &= C_0(t) + \langle I^i_{\mathrm{ref}}(t)[B^i_{\mathrm{noise}} - \langle B^i_{\mathrm{noise}}\rangle_N]\rangle_N. \end{aligned} \quad \text{(D3)}$$

Because of the random statistical nature of noise and the absence of correlation between the noise and the incident reference signal, the second term is approximately zero. Therefore, the quality of the ghost image is almost independent of the noise. This explains why TGI is robust with regard to noise.

[1] J. H. Erkmen and Baris I. Shapiro, Ghost imaging: From quantum to classical to computational, Adv. Opt. Photonics **2**, 405 (2010).

[2] T. B. Pittman, Y. H. Shih, D. V. Strekalov, and A. V. Sergienko, Optical imaging by means of two-photon quantum entanglement, Phys. Rev. A **52**, R3429 (1995).

[3] R. S. Bennink, S. J. Bentley, and R. W. Boyd, Coincidence Imaging with a Classical Source, Phys. Rev. Lett. **89**, 9 (2002).

[4] R. S. Bennink, S. J. Bentley, R. W. Boyd, and J. C. Howell, Quantum and Classical Coincidence Imaging, Phys. Rev. Lett. **92**, 033601 (2004).

[5] F. Ferri, D. Magatti, A. Gatti, M. Bache, E. Brambilla, and L. A. Lugiato, High-resolution Ghost Image and Ghost Diffraction Experiments with Thermal Light, Phys. Rev. Lett. **94**, 2 (2005).

[6] D. Pelliccia, A. Rack, M. Scheel, V. Cantelli, and D. M. Paganin, Experimental X-Ray Ghost Imaging, Phys. Rev. Lett. **117**, 113902 (2016).

[7] H. Yu, R. Lu, S. Han, H. Xie, G. Du, T. Xiao, and D. Zhu, Fourier-Transform Ghost Imaging with Hard X Rays, Phys. Rev. Lett. **117**, 113901 (2016).

[8] A. I. I. N. Z. Hang, Y. U. H. E. Ang, L. N. W. U. Ing, and L. I. I. N. G. C. Hen, Tabletop x-ray ghost imaging with ultra-low radiation, Optica **5**, 4 (2018).

[9] R. I. Khakimov, B. M. Henson, D. K. Shin, S. S. Hodgman, R. G. Dall, K. G. H. Baldwin, and A. G. Truscott, Ghost imaging with atoms, Nature **540**, 100 (2016).

[10] S. Li, F. Cropp, K. Kabra, T. J. Lane, G. Wetzstein, P. Musumeci, and D. Ratner, Electron Ghost Imaging, Phys. Rev. Lett. **121**, 114801 (2018).

[11] J. H. Shapiro, Computational ghost imaging, Phys. Rev. A **78**, 061802 (2008).

[12] P. Ryczkowski, M. Barbier, A. T. Friberg, J. M. Dudley, and G. Genty, Ghost imaging in the time domain, Nat. Photonics **10**, 167 (2016).

[13] K. Cho and J. Noh, Temporal ghost imaging of a time object, dispersion cancelation, and nonlocal time lens with bi-photon state, Opt. Commun. **285**, 1275 (2012).

[14] Z. Chen, H. Li, Y. Li, J. Shi, and G. Zeng, Temporal ghost imaging with a chaotic laser, Opt. Eng. **52**, 076103 (2013).

[15] H. Wu, P. Ryczkowski, A. T. Friberg, J. M. Dudley, and G. Genty, Temporal ghost imaging using wavelength conversion and two-color detection, Optica **6**, 902 (2019).

[16] F. Devaux, P.-A. Moreau, S. Denis, and E. Lantz, Computational temporal ghost imaging, Optica **3**, 2 (2016).

[17] N. D. Hardy and J. H. Shapiro, Computational ghost imaging versus imaging laser radar for three-dimensional imaging, Phys. Rev. A **87**, 023820 (2013).

[18] H. C. Liu, B. Yang, Q. Guo, J. Shi, C. Guan, G. Zheng, H. Mühlenbernd, G. Li, T. Zentgraf, and S. Zhang, Single-pixel computational ghost imaging with helicity-dependent metasurface hologram, Sci. Adv. **3**, 4 (2017).

[19] P. Janassek, S. Blumenstein, and W. Elsäßer, Ghost Spectroscopy with Classical Thermal Light Emitted by a Superluminescent Diode, Phys. Rev. Appl. **9**, 021001 (2018).

[20] P. A. Morris, R. S. Aspden, J. E. C. Bell, R. W. Boyd, and M. J. Padgett, Imaging with a small number of photons, Nat. Commun. **6**, 1 (2015).

[21] R. H. Wiley and D. G. Richards, Physical constraints on acoustic communication in the atmosphere: Implications for the evolution of animal vocalizations, Behav. Ecol. Sociobiol. **3**, 69 (1978).

[22] P. L. Carson, C. R. Meyer, A. L. Scherzinger, and T. V. Oughton, Breast imaging in coronal planes with simultaneous pulse echo and transmission ultrasound, Science **214**, 1141 (1981).

[23] A. Fenster and D. B. Downey, 3-D ultrasound imaging: A review, IEEE Eng. Med. Biol. Mag. **15**, 41 (1996).

[24] P. Kruizinga, P. Van Der Meulen, A. Fedjajevs, F. Mastik, G. Springeling, N. De Jong, J. G. Bosch, and G. Leus, Compressive 3D ultrasound imaging using a single sensor, Sci. Adv. **3**, e1701423 (2017).

[25] C. Ma, S. Kim, and N. X. Fang, Far-field acoustic subwavelength imaging and edge detection based on spatial filtering and wave vector conversion, Nat. Commun. **10**, 204 (2019).

[26] R. Piotr, Magnified time-domain ghost imaging, APL Photonics **2**, 046102 (2017).

[27] Y. O-Oka and S. Fukatsu, Differential ghost imaging in time domain, Appl. Phys. Lett. **111**, 061106 (2017).

[28] B. Sun, S. S. Welsh, M. P. Edgar, J. H. Shapiro, and M. J. Padgett, Normalized ghost imaging, Opt. Express **20**, 16892 (2012).

[29] O. Katz, Y. Bromberg, and Y. Silberberg, Compressive ghost imaging, Appl. Phys. Lett. **95**, 131110 (2009).

[30] C. Zhang, S. Guo, J. Cao, J. Guan, and F. Gao, Object reconstitution using pseudo-inverse for ghost imaging, Opt. Express **22**, 30063 (2014).

[31] R. E. Meyers, K. S. Deacon, and Y. Shih, Turbulence-free ghost imaging, Appl. Phys. Lett. **98**, 111115 (2011).

[32] M. Bina, D. Magatti, M. Molteni, A. Gatti, L. A. Lugiato, and F. Ferri, Backscattering Differential Ghost Imaging in Turbid Media, Phys. Rev. Lett. **110**, 083901 (2013).

[33] Y.-K. Xu, W.-T. Liu, E.-F. Zhang, Q. Li, H.-Y. Dai, and P.-X. Chen, Is ghost imaging intrinsically more powerful against scattering?, Opt. Express **23**, 32993 (2015).

[34] S. Denis, P. A. Moreau, F. Devaux, and E. Lantz, Temporal ghost imaging with twin photons, J. Opt. **19**, 034002 (2017).

[35] F. Devaux, K. P. Huy, S. Denis, E. Lantz, and P. A. Moreau, Temporal ghost imaging with pseudo-thermal speckle light, J. Opt. **19**, 024001 (2017).

[36] J. Tang, D. Zou, M. Cheng, L. Deng, D. Liu, and M. Zhang, Single-shot temporal ghost imaging based on orthogonal frequency-division multiplexing, IEEE Photonics Technol. Lett. **30**, 1555 (2018).

[37] S. Jiang, Y. Wang, T. Long, X. Meng, X. Yang, R. Shu, and B. Sun, Information security scheme based on computational temporal ghost imaging, Sci. Rep. **7**, 1 (2017).

[38] K. Yi, Z. Leihong, and Z. Dawei, Study of an encryption system based on compressive temporal ghost imaging with a chaotic laser, Opt. Commun. **426**, 535 (2018).